

Monte Carlo renormalization group study of the Heisenberg and the XY antiferromagnet on the stacked triangular lattice and the chiral ϕ^4 model

M. Itakura

JST, Center for Promotion of Computational Science and Engineering, Japan Atomic Energy Research Institute, Meguro-ku, Nakameguro 2-2-54, Tokyo 153, Japan

(December 2, 2024)

With the help of the improved Monte Carlo renormalization-group scheme, we numerically investigate the renormalization group flow of the antiferromagnetic Heisenberg and XY spin model on the stacked triangular lattice (STA-model) and its effective Hamiltonian, $2N$ -component chiral ϕ^4 model which is used in the field-theoretical studies. We find that the XY-STA model with lattice size $84 \times 96 \times 84$ exhibits clear first-order behavior. We also find that the renormalization-group flow of the STA model is well reproduced by the chiral ϕ^4 model, and that there are no chiral fixed point of renormalization-group flow for $N = 2$ and 3 cases. This result indicates that the Heisenberg-STA model also undergoes first-order transition.

PACS numbers: 75.10.Nr

I. INTRODUCTION

The critical behavior of the antiferromagnetic vector spin models on the stacked triangular lattice (STA) is still a controversial issue even after twenty years of extensive studies by means of experimental, field-theoretical, and numerical methods. See¹⁻⁵ for recent works, and⁶ for a review.

The field-theoretical renormalization group (RG) analysis tells that when the number of spin component N is greater than some threshold value N_c , there are so-called "chiral fixed point" of the RG which controls the critical behavior and is characterized by novel values of critical exponents, while for $N < N_c$ such fixed point disappears and the phase transition is of first order (see⁶ for a review). Theoretical estimations of N_c have been made by various authors by means of ϵ -expansion^{2,7,8}, fixed dimensional perturbation^{2,3,9}, local potential approximation¹⁰, and effective average action approach¹, but the estimated values ranges from negative value to 6.5, depending on the method employed (however, recent results tend to be around 6.0). Thus the critical behavior of the physical relevant cases $N = 2$ (XY spin) and $N = 3$ (Heisenberg spin) is still unclear. A number of experimental studies⁴ and numerical simulations^{11,12} have yielded results which suggest second-order phase transition for $N = 2$ and 3. However, recently it has been pointed out that the critical exponent η calculated from scaling relation becomes negative in some of these results, which is unphysical and indicates that the observed critical behavior is in fact pseudo-critical behavior induced by the slow RG flow^{1,5,10}.

The present work intends to clarify the issue by numerically observing the RG flow and investigating whether there are chiral fixed point or not for several values of N . The paper

is organized as follows. In the next section, we will present the method by which we observe the RG flow in the Monte Carlo simulations. Details of the Monte Carlo simulations are given in Sec. III. In Sec. IV the RG flow obtained from the simulations for $N = 2, 3, 8$ cases are presented. The last section is devoted to the concluding remarks.

II. NUMERICAL OBSERVATION OF THE RG FLOW

A. chiral ϕ^4 model

The critical behavior of the N -component STA models are essentially described by the following $2N$ -component Ginzburg-Landau-Wilson Hamiltonian⁶:

$$H = \int dx \left[K \left((\nabla \vec{\phi}_a)^2 + (\nabla \vec{\phi}_b)^2 \right) + r \left(\vec{\phi}_a^2 + \vec{\phi}_b^2 \right) + u \left(\vec{\phi}_a^2 + \vec{\phi}_b^2 \right)^2 + v \left((\vec{\phi}_a \cdot \vec{\phi}_b)^2 - \vec{\phi}_a^2 \vec{\phi}_b^2 \right) \right], \quad (1)$$

where $\vec{\phi}_a$ and $\vec{\phi}_b$ are N -component vector defined on the continuum space. In the field-theoretical studies, K is fixed to unity to eliminate ambiguity of coefficients induced by a trivial rescaling of ϕ , namely, $\vec{\phi} \rightarrow c\vec{\phi}$. In this regularization scheme, r plays a role of temperature. In the present work we concentrate on the case $v \geq 0$. The renormalization group flow of r , u , and v becomes the one shown in Fig. 1. Above the critical plane, the flow is attracted to the high-temperature fixed point $(r, u, v) = (\infty, 0, 0)$. Below the critical plane, if $v > 0$, the flow is attracted to the anisotropic low-temperature fixed point $(-\infty, \infty, \infty)$, while on the isotropic plane $v = 0$, the flow is attracted to the isotropic low-temperature fixed point $(-\infty, \infty, 0)$. The flow on the critical plane projected onto the u - v plane is shown in Fig. 2 for (a) $N < N_c$ and (b) $N > N_c$ cases. When $N > N_c$, there are stable and unstable chiral fixed points denoted by C_1 and C_2 , respectively, beside the $O(2N)$ symmetric and the Gaussian fixed points denoted by O and G, respectively. The two fixed points C_1 and C_2 approach as N decreases, and annihilate each other at $N = N_c$.

To observe the RG flow directly from the numerical simulation, we use the lattice version of the Hamiltonian (1):

$$H = \frac{K}{2} \sum_{\langle ij \rangle} (\vec{\phi}(i) - \vec{\phi}(j))^2 + r \sum_i \vec{\phi}(i)^2 + u \sum_i (\vec{\phi}(i)^2)^2 + v \sum_i [(\vec{\phi}_a(i) \cdot \vec{\phi}_b(i))^2 - \vec{\phi}_a(i)^2 \vec{\phi}_b(i)^2], \quad (2)$$

where $\vec{\phi}(i) = (\vec{\phi}_a(i), \vec{\phi}_b(i))$ is an $N + N$ -component vector defined on the lattice site i of $L \times L \times L$ cubic lattice with periodic boundary condition being imposed, the summation $\sum_{\langle ij \rangle}$ runs over all nearest neighbor pairs of the lattice site. In the numerical simulations, we use a restriction $u + v/4 - 2r = 0$ so that the minimum of the Hamiltonian takes place at $|\vec{\phi}(i)| = 1$, which removes the ambiguity of the trivial rescaling of ϕ . Actually we use the following parameterization:

$$r = -2\lambda, \quad u = \lambda(1 + A), \quad v = 4\lambda A \quad (3)$$

where A controls the strength of the anisotropy and λ controls the "hardness" of the spin—the larger λ is, the smaller the fluctuation of $|\vec{\phi}(i)|$ is. A line $\lambda = 0$ corresponds to $u-v/4 = 0$, on which instability of the Hamiltonian (2) occurs. Thus λ should be positive.

By means of Monte Carlo simulation, we calculate the following quantities:

$$C_L = \frac{\langle \vec{M}(\mathbf{k}_1) \cdot \vec{M}(-\mathbf{k}_1) \rangle}{\langle \vec{M}^2 \rangle}, \quad (4)$$

$$U_L = \frac{\langle (\vec{M}^2)^2 \rangle}{\langle \vec{M}^2 \rangle^2}, \quad (5)$$

$$V_L = \frac{\langle \vec{M}_a^2 \vec{M}_b^2 - (\vec{M}_a \cdot \vec{M}_b)^2 \rangle}{\langle \vec{M}^2 \rangle^2}, \quad (6)$$

where $\vec{M}_a = \sum_i \vec{\phi}_a(i)$, $\vec{M}_b = \sum_i \vec{\phi}_b(i)$, $\vec{M} = \sum_i \vec{\phi}(i)$, $\vec{M}(\mathbf{k}_1) = \sum_{\mathbf{r}} \exp(i\mathbf{k}_1 \cdot \mathbf{r})$ with $\mathbf{k}_1 = (2\pi/L, 0, 0)$, and the symbol $\langle \rangle$ denotes thermal average in the $L \times L \times L$ lattice. C_L , U_L and V_L are thermal averages of the first, third, and fourth term, respectively, of (2) in the renormalized Hamiltonian¹³. If one plot (U_L, V_L, C_L) for fixed values of A , λ , K and increasing values of L , the point moves along the arrows shown in Fig. 3. A number of trivial fixed points, namely, high-temperature fixed point $(1 + 1/2N, \frac{(2N+1)(N-1)}{8N(N+1)}, 1)$, isotropic low-temperature fixed point $(1, \frac{N-1}{4(N+1)}, 0)$, and anisotropic low-temperature fixed point $(1, \frac{1}{4}, 0)$ are denoted by H, L_0 , and L_1 , respectively. If the probability distribution of the order parameter \vec{M} is isotropic, a relation $V_L = \frac{N-1}{4(N+1)}U_L$ is satisfied, while in the strong anisotropy limit where $\vec{M}_a \cdot \vec{M}_b = 0$ and $|\vec{M}_a| = |\vec{M}_b|$ hold, $V_L = U_L/4$ is satisfied. At the Gaussian fixed point, the behavior of the finite system is governed by the zero-mode¹³, therefore the Gaussian fixed point lies on the $C_L = 0$ plane. The RG flow on the critical plane, projected onto the U_L - V_L plane, is shown in Fig. 4 for (a) $N < N_c$ and (b) $N > N_c$ cases. In both cases, the RG flow along the (approximately) horizontal direction rapidly converges, while along the (approximately) vertical direction the flow is expected to slowly converge/diverge.

In the present work, we assume that there are only three scaling variables which is essential for the phase transition, and that the three quantities U_L , V_L , and C_L well reflects the scaling behavior of these three scaling variables. Other scaling variables associated to the higher order term such as $|\phi|^6$, $|\phi|^8$, \dots are assumed to be irrelevant at the critical point and that they rapidly vanish as L increases. However, at the strong first-order transition region, these higher order terms becomes non-negligible and induce systematic error in the U_L - V_L plot. Therefore we will omit the data of strong first-order region from the U_L - V_L plot.

To obtain the RG flow on the critical plane, one must define the critical temperature K_c for each set of parameters A and λ . In the present work, we use size-dependent critical temperature K_c defined as follows: For a given value of λ , A and two different system sizes $L_1 < L_2$, K_c is defined as that at which $C_{L_1}(K_c) = C_{L_2}(K_c)$ is satisfied. Then one draw a line from $(U_{L_1}(K_c), V_{L_1}(K_c))$ to $(U_{L_2}(K_c), V_{L_2}(K_c))$ for various values of A and λ , then the RG flow diagram shown in Fig. 4 is obtained. It should be noted that the above definition of K_c induces systematic deviation. For example, consider the RG flow of the isotropic ϕ^4 model (set $v = 0$ in (2)). The flow of (U_L, C_L) near the Wilson-Fisher fixed point is depicted in Fig. 5 (a)¹³. If one define K_c by $C_{L_1}(K_c) = C_{L_2}(K_c)$, the flow of $U_L(K_c)$ becomes the one

shown in Fig. 5(b), thus the arrow tends to “overshoot” the RG fixed point. However, the direction of the flow can be correctly estimated, and the systematic error vanishes as one approaches the fixed point.

B. STA models

We also observe the RG flow of the following STA model:

$$H = -K \sum_{\langle ij \rangle} J_{ij} \vec{S}_i \cdot \vec{S}_j, \quad (7)$$

where \vec{S}_i denotes two-component (XY) or three-component (Heisenberg) vector with $|\vec{S}_i| = 1$ defined on the lattice site i of the stacked triangular lattice. We set $J_{ij} = -1$ (antiferromagnetic) for intra-plane nearest neighbor pairs, $J_{ij} = 3/4$ (ferromagnetic) for inter-plane nearest neighbor pairs, and $J_{ij} = 0$ otherwise, so that the Fourier transform of J_{ij} near the antiferromagnetic mode¹⁴ $\vec{k}_{AF} = (2\pi/3, 0, 0)$ becomes isotropic in the \vec{k} -space, i.e. $J(\vec{k}_{AF} + \vec{k}) \sim J(\vec{k}_{AF}) + c|\vec{k}|^2 + O(|\vec{k}|^4)$. Note that the critical values of quantities such as U_L, V_L , and C_L do not depend on the microscopic lattice structure, but *do* depend on the macroscopic lattice structure such as boundary conditions and aspect ratios^{15,16}. Therefore we use rectangular system which contains $L_x \times L_y \times L_z$ spins (see Fig. 6), imposing periodic boundary condition for all three directions. The aspect ratio then becomes $L_x : \sqrt{3}L_y/2 : L_z$. We simulate the system with $(L_x, L_y, L_z) = (21, 24, 21)$, $(42, 48, 42)$, and $(84, 96, 84)$, all of which gives aspect ratio 1 : 0.99 : 1.

The order parameter is defined as follows⁶:

$$\vec{M}_a = \text{Re}[\vec{S}(\vec{k}_{AF})] = \vec{M}_A - \frac{1}{2}\vec{M}_B - \frac{1}{2}\vec{M}_C, \quad (8)$$

$$\vec{M}_b = \text{Im}[\vec{S}(\vec{k}_{AF})] = \frac{\sqrt{3}}{2}\vec{M}_B - \frac{\sqrt{3}}{2}\vec{M}_C, \quad (9)$$

where $\vec{S}(\vec{k}_{AF})$ denotes Fourier component of \vec{S}_i at \vec{k}_{AF} , and $\vec{M}_A, \vec{M}_B, \vec{M}_C$ denote the magnetization on the three sublattices. Then U_L and V_L are calculated from Eq. (5) and Eq. (6). C_L is calculated as follows:

$$C_L = \frac{\langle |\vec{S}(\vec{k}_{AF} + \vec{k}_1)|^2 + |\vec{S}(\vec{k}_{AF} - \vec{k}_1)|^2 \rangle}{\langle \vec{S}^2(0) \rangle}, \quad (10)$$

where \vec{k}_1 is the smallest, non-zero momentum in the \vec{k} -space. We observed the values of C_L for three kinds of direction, namely, $\vec{k}_1 = (\frac{2\pi}{L_x}, 0, 0)$, $(0, \frac{4\pi}{\sqrt{3}L_y}, 0)$, and $(0, 0, \frac{2\pi}{L_z})$, and confirmed that they coincide each other within statistical errors. This indicates that the simulated system is isotropic.

III. MONTE CARLO SIMULATION

A. chiral ϕ^4 models

We use single-spin update Metropolis algorithm, since there are no spin reflection axis which preserves the anisotropy term in (2), therefore the cluster algorithm¹⁷ cannot be applied. In a single-spin update process, the new spin value is chosen as follows:

$$\vec{\phi}_{new}(i) = \vec{\phi}_{old}(i) + \frac{R_g}{\sqrt{2N}} \vec{G} \quad (11)$$

where \vec{G} is an $2N$ -component vector whose components are independent Gaussian random variables with average 0 and variance 1. R_g is the amplitude of random variables, whose optimum value is determined by simulating small systems to minimize the autocorrelation. The optimum value is found to be $R_g \approx 0.3$ for all N , A , and λ . Each Metropolis sweep is followed by one overrelaxation-type update¹⁸. Hereafter we refer one Metropolis sweep plus one overrelaxation-type sweep as ‘‘MCS’’.

Physical quantities are observed for every $C_{INT} \times L^2$ MCS, where C_{INT} is a constant which depends on N , λ , and A , but not on L : this constant is adjusted so that the autocorrelation of all the successively observed quantities becomes less than 0.70, namely:

$$\frac{\langle X_t X_{t+1} \rangle - \langle X_t \rangle^2}{\langle X_t^2 \rangle - \langle X_t \rangle^2} < 0.7, \quad (12)$$

where X_t denotes observed value of a physical quantity X at the t th observation. The value of C_{INT} ranges from 0.1 to 2.0, and mainly depends on A . Actual values are summarized in the later sections. For each values of L , N , A , and λ , physical quantities are observed from 10^4 to 10^5 times, depending on the accuracy required to observe the RG flow. Statistical errors are estimated from the Jackknife method. Histogram method¹⁹ is used to calculate thermal averages at K slightly away from that at which the simulation is actually carried out.

Simulations are mainly carried out on Fujitsu VPP5000 vector processors at JAERI. The checkerboard-wise decomposition of the lattice is used for vectorization. Furthermore, we simultaneously simulate a number of independent systems, whose spins are stored into one long vector. This promotes the vectorization, especially when L is small, and accelerates the calculations. For $N = 8$ and $L = 16$ system, one MCS take 0.84 ms on the VPP5000.

B. STA models

In the frustrated spin models, the cluster update algorithm tends to flip all the spins and does not accelerate the simulation. Therefore we use single-spin update Metropolis algorithm, followed by an overrelaxation sweep, i.e. 180 degree rotation of spin \vec{S}_i with respect to its local field $\sum_j J_{ij} \vec{S}_j$. In the Metropolis update, the new spin direction is chosen as

$$S_x = \sqrt{1 - z^2} \cos(\theta), \quad S_y = \sqrt{1 - z^2} \sin(\theta), \quad S_z = z \quad (13)$$

for Heisenberg case and

$$S_x = \cos(\theta), \quad S_y = \sin(\theta) \quad (14)$$

for XY case, where z and θ are uniformly distributed random number in the range $[-1, 1)$ and $[0, 2\pi)$, respectively. Physical quantities are observed for every $L_x \times L_y/20$ MCS for Heisenberg case and $L_x \times L_y/10$ MCS for XY case. In these intervals, the system decorrelates and the condition (12) is satisfied for all system sizes. For the largest system size $(L_x, L_y, L_z) = (84, 96, 84)$, physical quantities are observed 0.5×10^4 times, and 10^4 times for other sizes. For $N = 3$ and $(L_x, L_y, L_z) = (84, 96, 84)$ system, one MCS takes 27 ms on the VPP5000.

C. Stiefel's $V_{N,2}$ models

Stiefel's $V_{N,2}$ model⁵ correspond to the Hamiltonian (2) with $\lambda = \infty$ and $A = \infty$, in which restrictions $\phi_a \cdot \phi_b = 0$, $\phi_a^2 = \phi_b^2 = 1/2$ are imposed to all the spins. We also simulate this model and investigate the RG flow. In the Monte Carlo simulation, only the Metropolis update is used. We only simulate the $V_{3,2}$ model, since the $V_{2,2}$ model is known to exhibit strong first-order behavior⁵. In this model, the new spin value is chosen as follows:

$$\vec{\phi}_a = (z, \sqrt{1-z^2} \cos \theta_1, \sqrt{1-z^2} \sin \theta_1)/\sqrt{2}, \quad (15)$$

$$\vec{\phi}_b = (\sqrt{1-z^2} \sin \theta_2, -\sin \theta_1 \cos \theta_2 - z \cos \theta_1 \sin \theta_2, \cos \theta_1 \cos \theta_2 - z \sin \theta_1 \sin \theta_2)/\sqrt{2} \quad (16)$$

where z and $\theta_{1,2}$ are uniformly distributed random number in the range $[-1, 1)$ and $[0, 2\pi)$, respectively. Physical quantities are observed for every L^2 Metropolis sweeps. In this interval, the system is well decorrelated and the condition (12) is satisfied for all system sizes. Observation is done 10^4 times for all system sizes. One Metropolis sweep of the $L = 48$ system takes 12.4 ms on the VPP5000.

IV. RESULTS

A. XY case

Parameters λ , A , and K at which simulations were carried out are summarized in Table I. Figure 7 shows the histogram of energy per spin $-\sum J_{ij} \vec{S}_i \vec{S}_j / L_x L_y L_z$ of the STA-XY model with $(L_x, L_y, L_z) = (84, 96, 84)$ at $K = 0.7725$. The double peak of the histogram is a clear evidence of first-order transition. This peak does not appear when the size is smaller, therefore the double peak has not been observed in the past studies of STA-XY model in which smaller systems has been used. Note that the first-order behavior has already been observed in the Monte Carlo simulations of other models which possess the same symmetry as the STA-XY model, such as Stiefel model and restricted STA model²⁰. These models have stronger anisotropy than the STA-XY model and the first-order behavior can be observed in smaller systems.

Figure 8 and 9 show the RG flow of (U_L, V_L) at the strong and weak anisotropy region, respectively, of the $N = 2$ chiral ϕ^4 model. Figure 8 also shows the same plot for the STA-XY model. One can see that the STA-XY model is on the “runaway” trajectory, which

is another evidence of first-order transition. It can also be seen that there are no stable fixed points other than the $O(4)$ symmetric one. This means that any models or materials which possess the same symmetry as STA-XY model, namely $Z_3 \times O(2)$, exhibits first-order transition.

Fig. 10 shows the vertical velocity of the RG flow $V_{2L} - V_L$ plotted against V_L . The plots for the two different sizes $L = 6$ and $L = 8$ coincide within statistical errors. This indicates that the system size is large enough to eliminate finite-size artifact of the RG flow. Thus we can safely extrapolate the asymptotic critical behavior from the finite-size RG flow. Moreover, the plots of the chiral ϕ^4 model and the STA-XY model are essentially the same. This means that the critical behavior if the STA-XY model is well reproduced by the chiral ϕ^4 model.

B. Heisenberg case

Parameters λ , A , and K at which simulations were carried out are summarized in Table II. Unlike the STA-XY case, neither the STA-Heisenberg model nor the $V_{3,2}$ model show the double-peak behavior within the simulated size, $(L_x, L_y, L_z) = (84, 96, 84)$ for STA-Heisenberg model and $L = 48$ for $V_{3,2}$ model.

Figure 11 and 12 show the RG flow of (U_L, V_L) at the strong and weak anisotropy region, respectively, of the $N = 3$ chiral ϕ^4 model. Figure 11 also shows the same plot for the STA-Heisenberg model and the $V_{3,2}$ model. It can be seen that the STA-Heisenberg model and the $V_{3,2}$ model are on the “runaway” trajectory, therefore undergoes first-order transition in the thermodynamic limit. It can also be seen that there are no fixed points other than the $O(6)$ symmetric one. This means that any models or materials which possess the same symmetry as STA-Heisenberg model, namely $Z_3 \times O(3)$, exhibits first-order transition.

Fig. 13 shows the vertical velocity of the RG flow $V_{2L} - V_L$ plotted against V_L . In this case, this quantity depends not only on V_L but also on U_L , although the dependence is not so strong. Therefore the plot can not be fitted to a single line well. However, there are no systematic deviation between the plots of the two different sizes. Thus we can safely extrapolate the asymptotic critical behavior from the finite-size RG flow. As in the XY case, the plots of the chiral ϕ^4 model and the STA-Heisenberg model are essentially the same and the critical behavior of the STA-Heisenberg model is well reproduced by the chiral ϕ^4 model.

C. $N = 8$ case

It is necessary to demonstrate that the MCRG scheme presented in Sec. II is able to detect the chiral fixed point if it does exist. For this purpose, we investigated $N = 8$ case, which is greater than any theoretical estimate of N_c in literature^{1-3,7-10}. Parameters λ , A , and K at which simulations were carried out are summarized in Table III. Figure 14 shows the RG flow of (U_L, V_L) for $L = 8 \rightarrow 16$. The stable chiral fixed point C_1 and the unstable chiral fixed point C_2 are clearly seen.

Fig. 15 shows the vertical velocity of the RG flow $V_{2L} - V_L$ plotted against V_L , using only the data near the stable fixed point C_1 . Unlike the $N = 2$ and the $N = 3$ case, this

plot has a zero. The plots of the two different size coincides within statistical error, which indicate that the simulated system is large enough to observe the RG flow.

V. CONCLUSION

The large scale Monte Carlo simulation of the STA-XY model have revealed that the transition is of first-order. This is the first numerical work to confirm the first-order transition of the simple STA-XY model. We have also investigated the RG flow the $2N$ -component chiral ϕ^4 model numerically and found that there are no chiral fixed point in $N = 2$ and $N = 3$ cases, and we conclude that the STA-Heisenberg model also undergoes first-order transition. For $N = 8$ case, we have found the chiral fixed points, thus the value of N_c is estimated as $3 < N_c < 8$. Further study to determine the precise value of N_c may be of some interest, because such a study will serve to test the accuracy of field theoretical techniques. However, once the nature of physical relevant case $N = 3$ and $N = 2$ is clarified, the precise value of N_c is of less importance.

VI. ACKNOWLEDGMENTS

The present author is grateful to D. Loison, B. Delamotte, and K. B. Varnashev for useful comments.

- ¹ M. Tissier, B. Delamotte, and D. Mouhanna, Phys. Rev. Lett.**84**, 5208 (2000); preprint, [cond-mat/0107183](#);[cond-mat/0101167](#).
- ² A. Pelissetto, P. Rossi and E. Vicari Phys. Rev. B**63** R140414 (2001); Nucl. Phys. B **607**, 605 (2001); preprint, [cond-mat/0106525](#).
- ³ K. B. Varnashev, preprint.
- ⁴ V. P. Plakhty, J. Kulda, D. Visser, E. V. Moskvina, and J. Wosnitza, Phys. Rev. Lett.**85**, 3942 (2000).
- ⁵ D. Loison and K. D. Schotte, Euro. Phys. J.B **14**, 125 (2000).
- ⁶ H. Kawamura, J. Phys.: Condens. Matter **10**, 4707 (1998).
- ⁷ H. Kawamura, J. Phys. Soc. Jpn.**59**, 2305 (1990).
- ⁸ S. A. Antonenko, A. I. Sokolov and K. B. Varnashev, Phys. Lett. A **208**, 161 (1995).
- ⁹ S. A. Antonenko and A. I. Sokolov, Phys. Rev. B**49**, 15901 (1994).
- ¹⁰ G. Zumbach, Phys. Rev. Lett.**71**, 2421 (1993); Nucl. Phys. B **413**, 771 (1994).
- ¹¹ H. Kawamura, J. Phys. Soc. Jpn.**61**, 1299 (1992).
- ¹² M. L. Plumer and A. Mailhot, Phys. Rev. B **50**, 16113 (1994).
- ¹³ M. Itakura, Phys. Rev. E**61**, 5924 (2000).
- ¹⁴ The first Brillouin zone is an (approximately regular) hexagon in the x - y plane and \vec{k}_{AF} is on the vertex of the hexagon.
- ¹⁵ K. Kaneda and Y. Okabe, Phys. Rev. Lett. **86**, 2134 (2001).
- ¹⁶ K. Kaneda, Y. Okabe, and M. Kikuchi, J. Phys. A **32**, 7263 (1999).

¹⁷ U. Wolff, Phys. Rev. Lett. **62**, 361 (1989).

¹⁸ M. Caselle and M. Hasenbusch, J. Phys. A **31**, 4603 (1998).

¹⁹ A. M. Ferrenberg and R. H. Swendsen, Phys. Rev. Lett. **61**, 2635 (1988).

²⁰ D. Loison and K. D. Schotte, Euro. Phys. J.B**5**, 735 (1998).

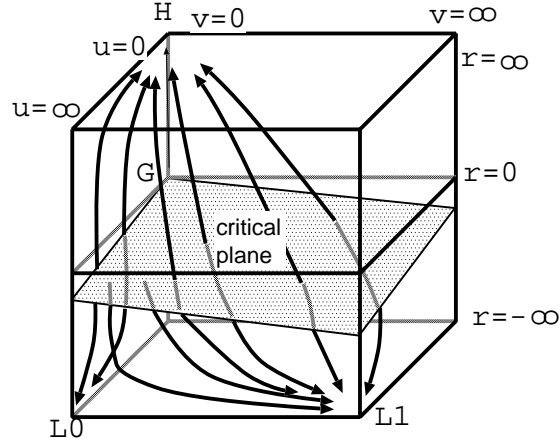


FIG. 1. Renormalization flow of r , u , and v . H, G, L₀, and L₁ denote the high-temperature, Gaussian, isotropic low-temperature, and anisotropic low-temperature fixed point, respectively.

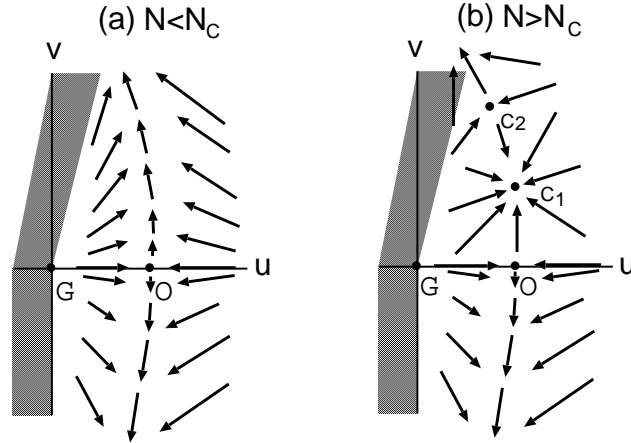


FIG. 2. Renormalization flow on the critical plane projected onto the u - v plane for (a) $N < N_c$ and (b) $N > N_c$. Shaded area is unstable region. G, O, C₁, and C₂ denote Gaussian, $O(2N)$ -isotropic, stable chiral, and unstable chiral fixed points, respectively.

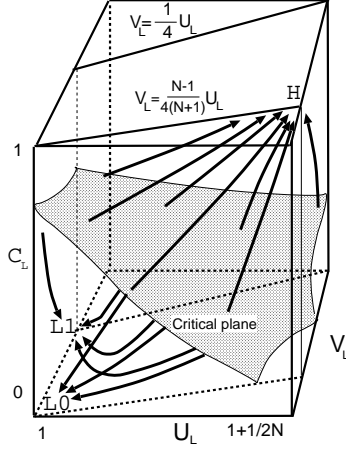


FIG. 3. Renormalization flow of C_L , U_L , and V_L .

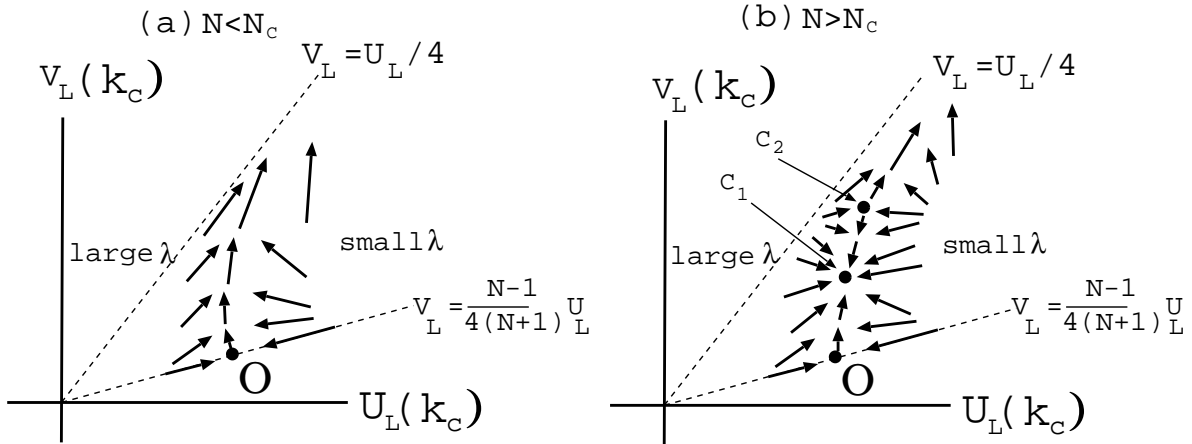


FIG. 4. Renormalization flow on the critical plane projected onto the U_L - V_L plane for (a) $N < N_c$ and (b) $N > N_c$ cases. The symbol O , C_1 , and C_2 denote $O(2N)$ -isotropic, stable chiral, and unstable chiral fixed point, respectively.

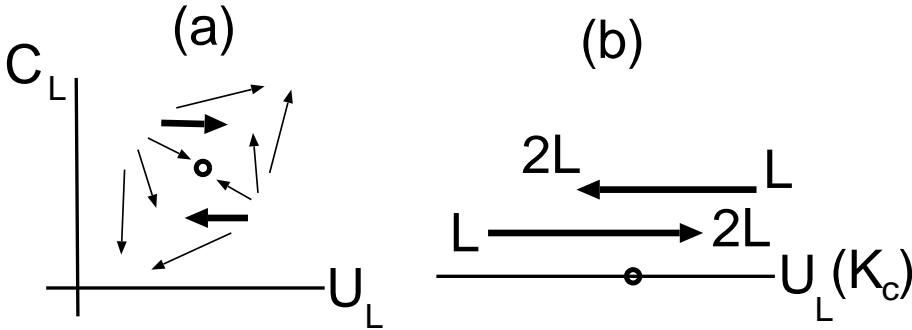


FIG. 5. (a) Renormalization flow of C_L and U_L for isotropic model $v = 0$ near the Wilson-Fisher fixed point. (b) RG flow of $U_L(K_c)$ tends to “overshoot” the fixed point (see the main text).

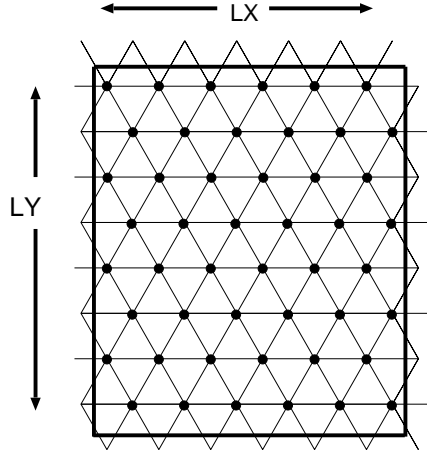


FIG. 6. Rectangular system used for the simulation of stacked triangular antiferromagnet. The figure shows a system with $L_x = 6, L_y = 8$. This layer is stacked L_z times.

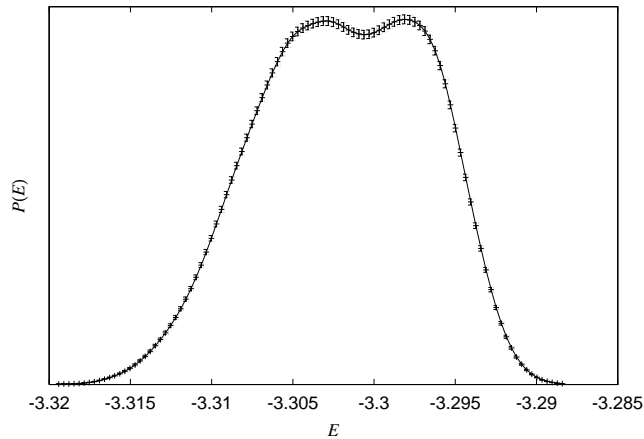


FIG. 7. Histogram of energy per spin of the STA-XY model with the size $(L_x, L_y, L_z) = (84, 96, 84)$ at $K = 0.7725$.

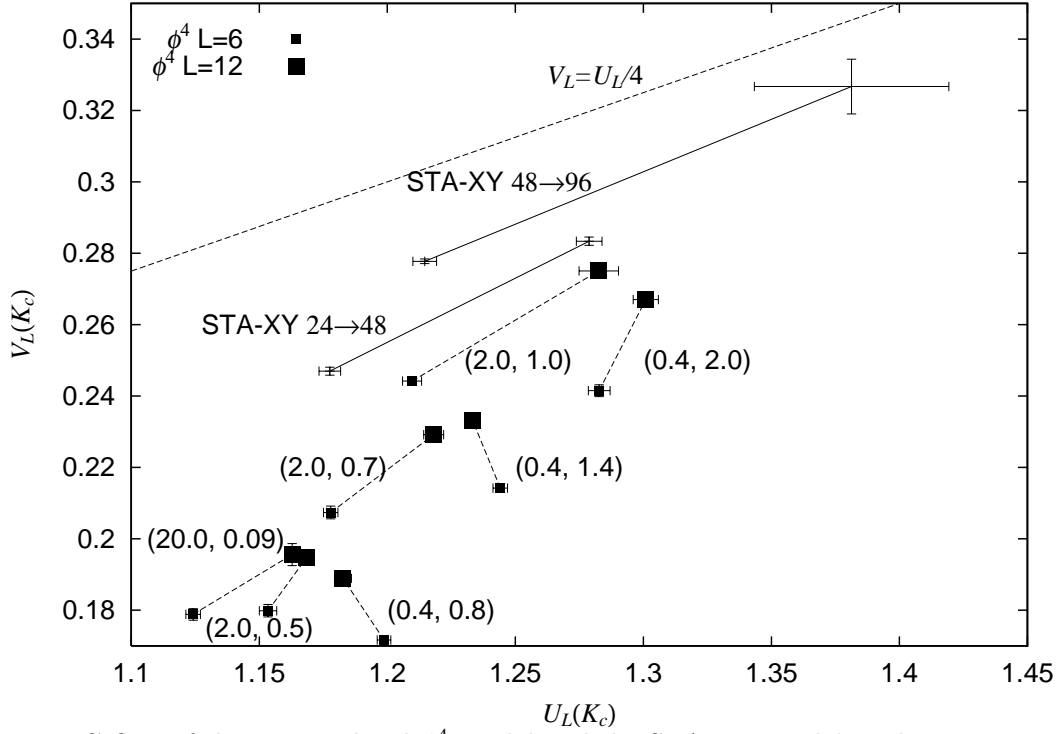


FIG. 8. RG flow of the $N = 2$ chiral ϕ^4 model and the STA-XY model at the strong anisotropy region. The numbers in parenthesis are the values of (λ, A) of the chiral ϕ^4 model.

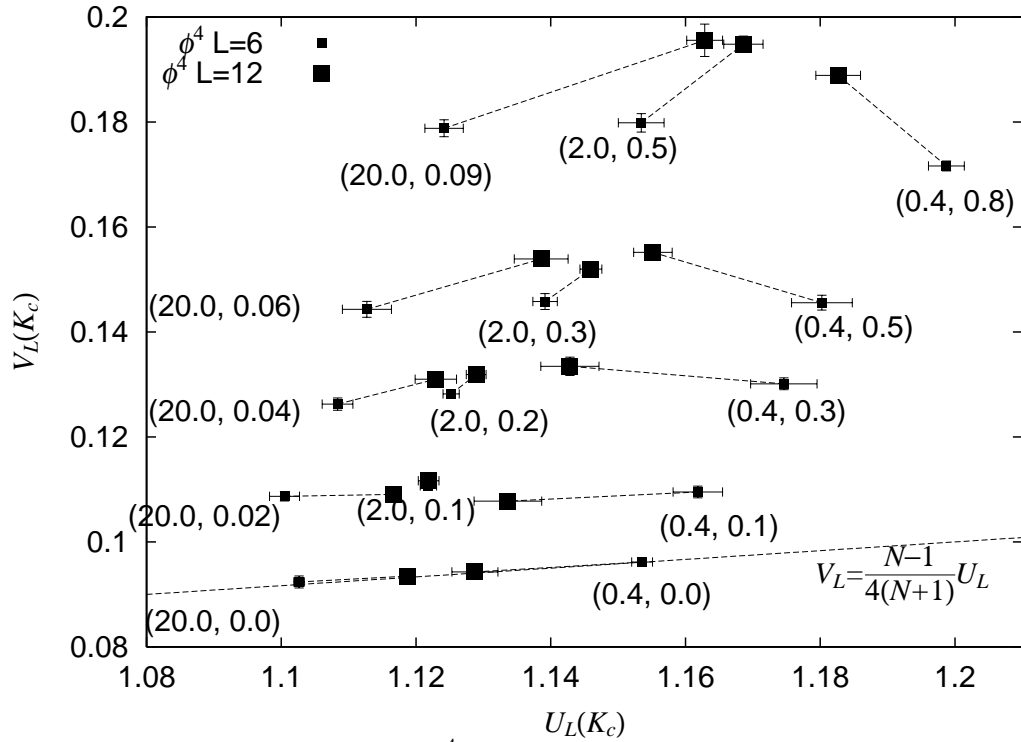


FIG. 9. RG flow of the $N = 2$ chiral ϕ^4 model at the weak anisotropy region. The numbers in parenthesis are the values of (λ, A) .

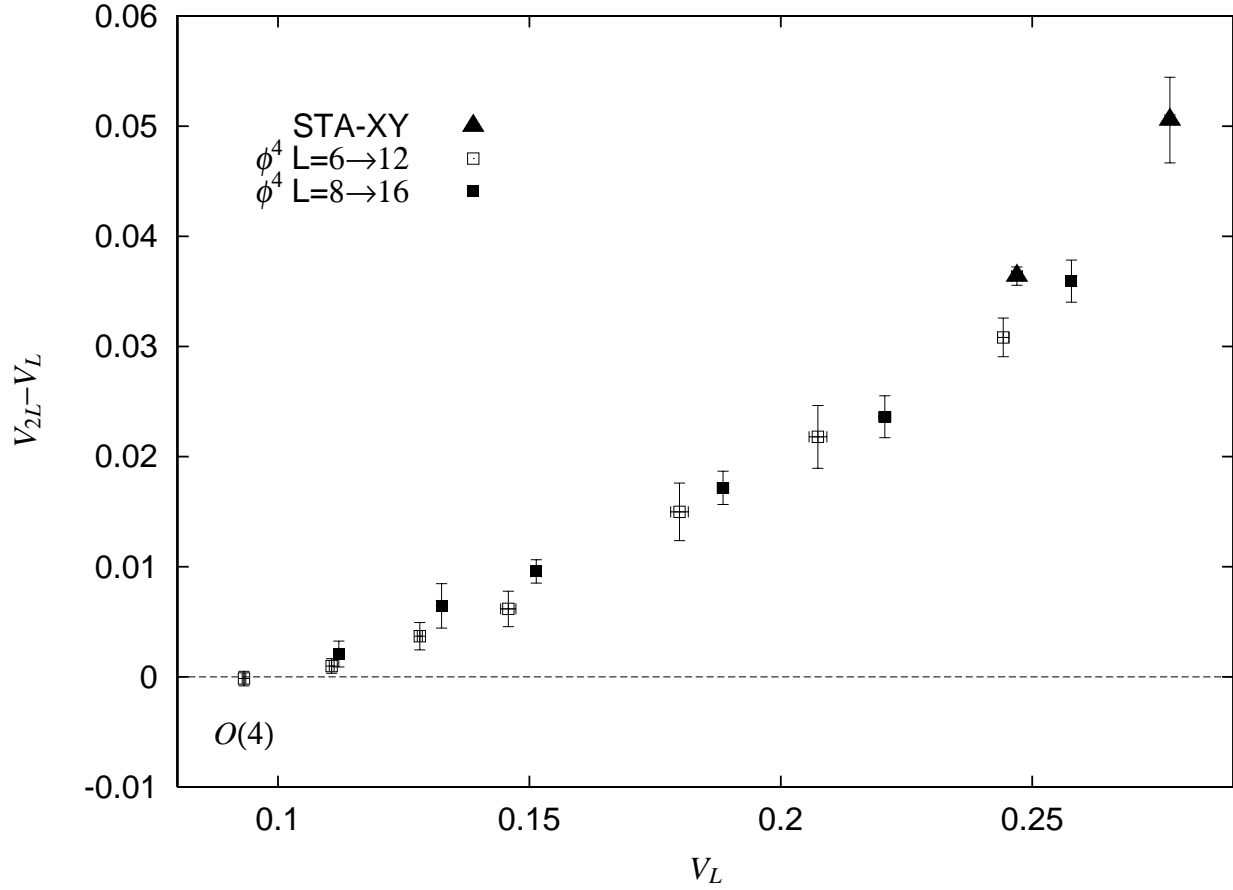


FIG. 10. The vertical velocity of the RG flow $V_{2L} - V_L$ against V_L for the $N = 2$ chiral ϕ^4 model and the STA-XY model. “ $O(4)$ ” denotes the $O(4)$ -symmetric fixed point.

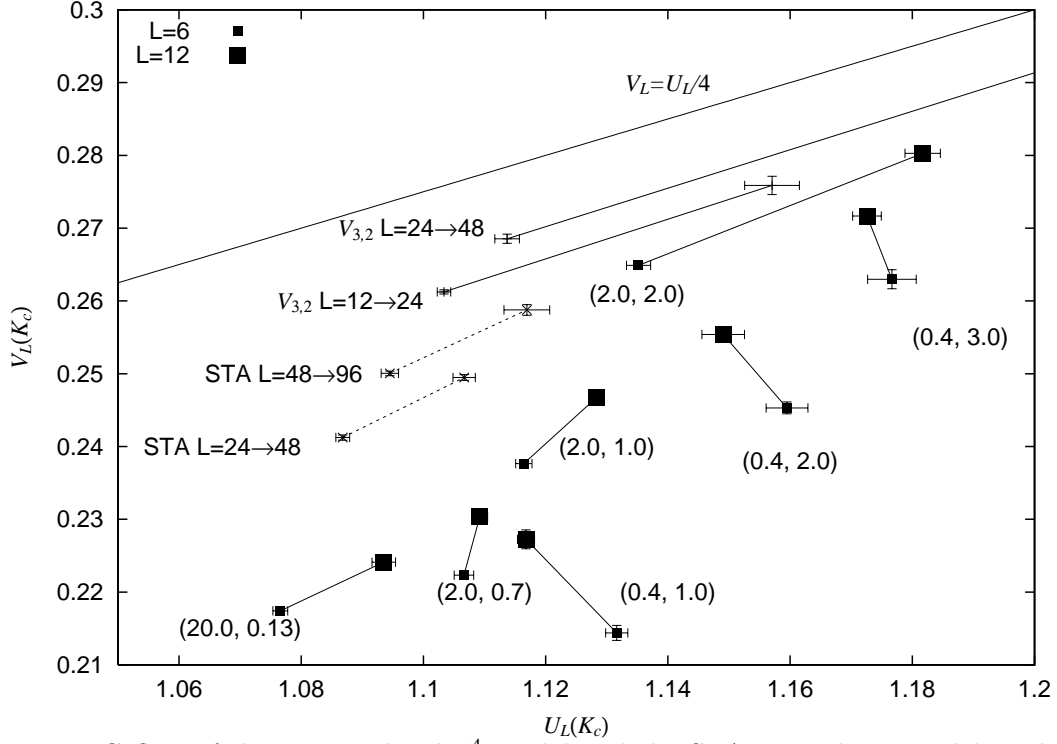


FIG. 11. RG flow of the $N = 3$ chiral ϕ^4 model and the STA-Heisenberg model at the strong anisotropy region. The numbers in parenthesis are the values of (λ, A) of the chiral ϕ^4 model.

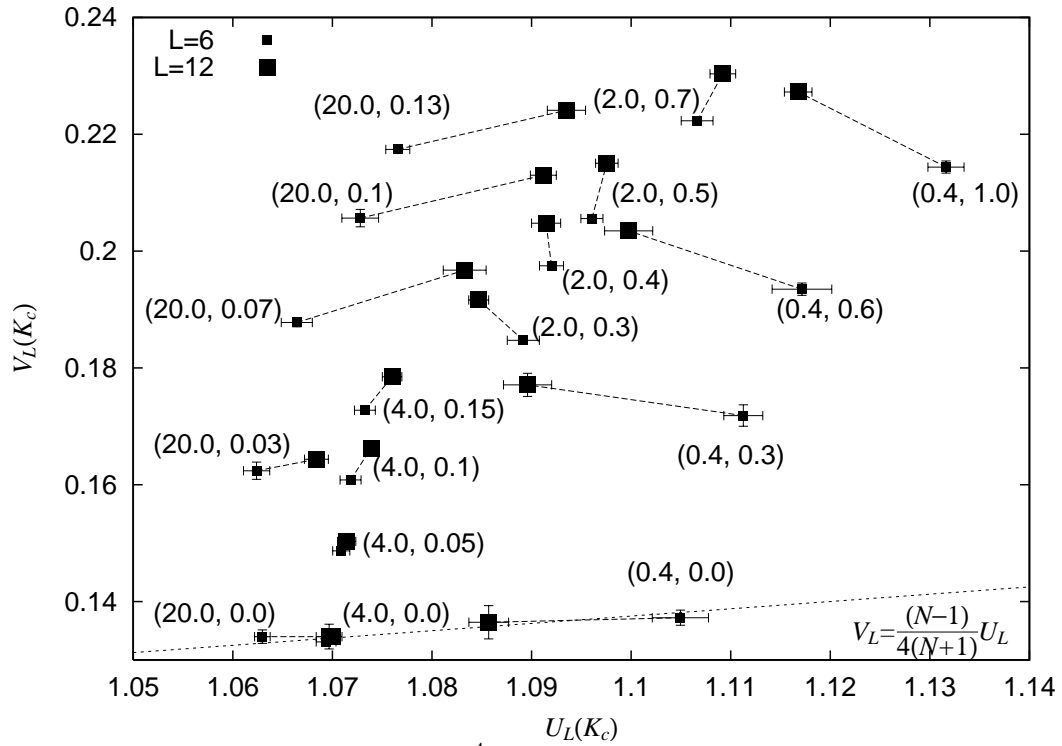


FIG. 12. RG flow of the $N = 3$ chiral ϕ^4 model at the weak anisotropy region. The numbers in parenthesis are the values of (λ, A) .

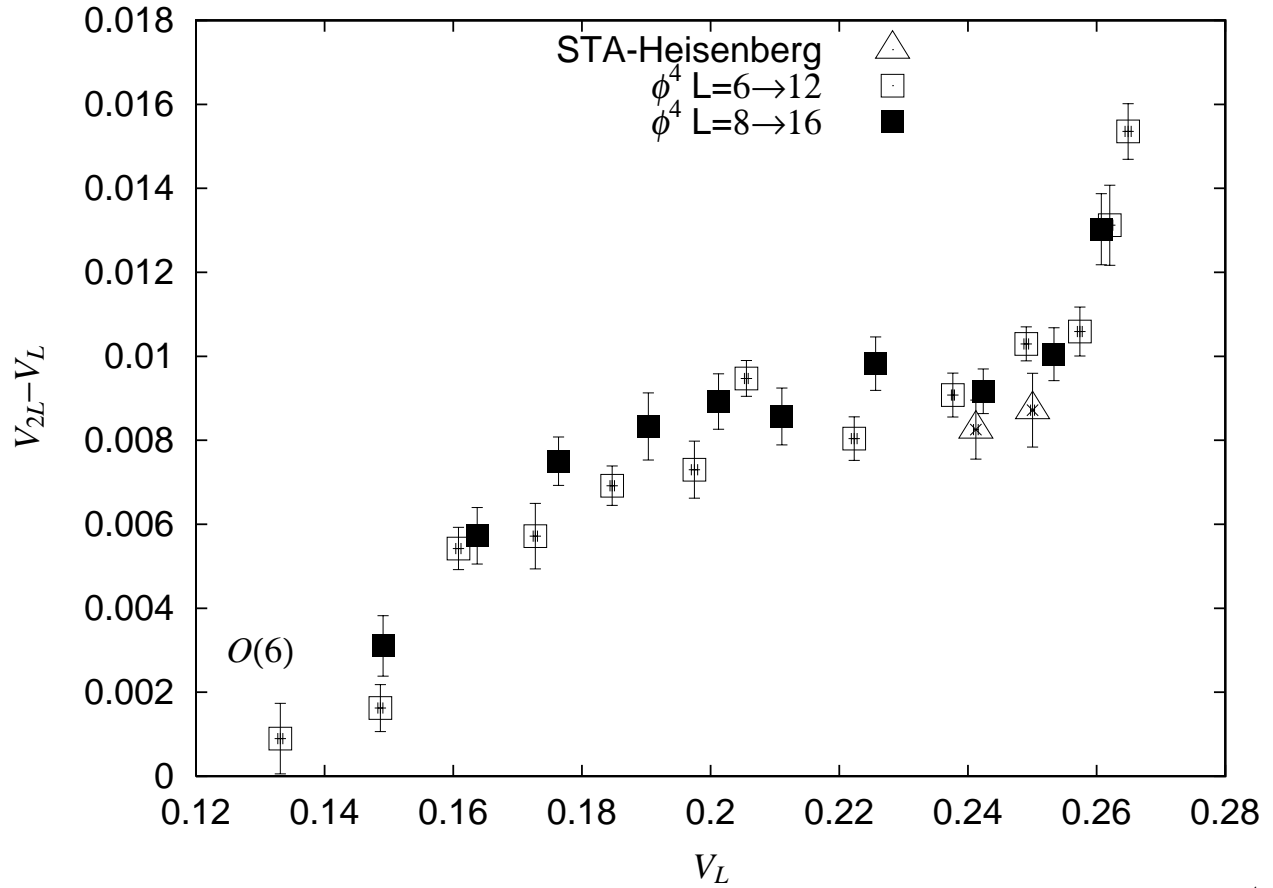


FIG. 13. The vertical velocity of the RG flow $V_{2L} - V_L$ against V_L for the $N = 3$ chiral ϕ^4 model and the STA-Heisenberg model. “ $O(6)$ ” denotes the $O(6)$ -symmetric fixed point.

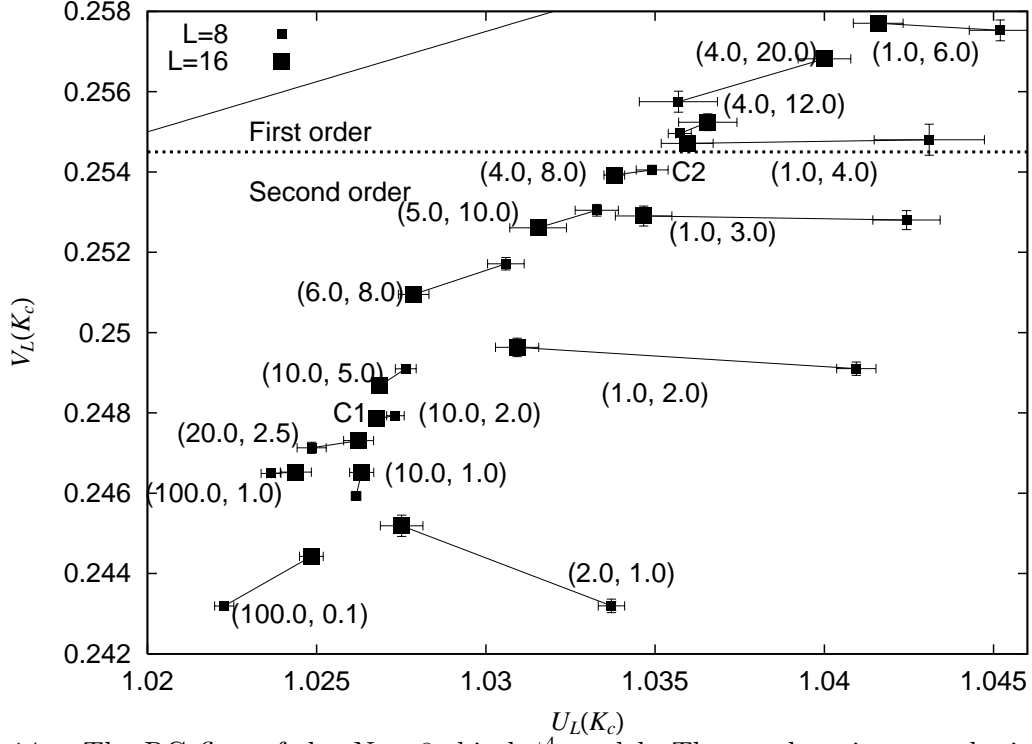


FIG. 14. The RG flow of the $N = 8$ chiral ϕ^4 model. The numbers in parenthesis show the values of (λ, A) . C1 and C2 denote the stable and unstable RG fixed point, respectively.

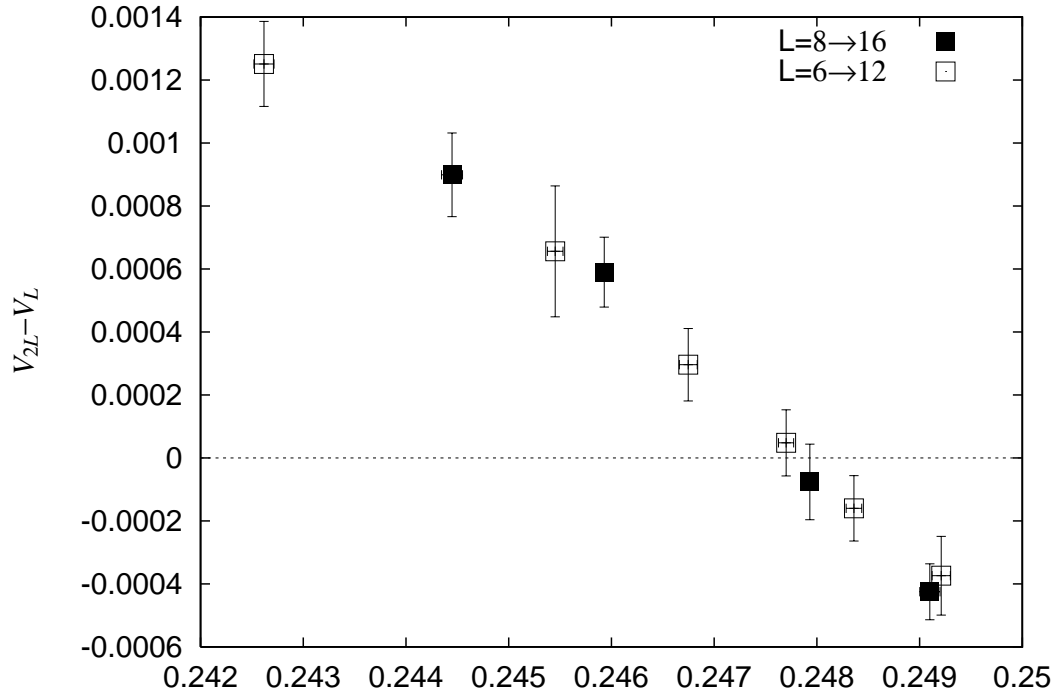


FIG. 15. The vertical velocity of the RG flow $V_{2L} - V_L$ against V_L near the stable chiral fixed point C_1 of the $N = 8$ chiral ϕ^4 model.

λ	A	K/N	C_{INT}
0.4	0.0	0.346	0.18
0.4	0.1	0.371	0.18
0.4	0.3	0.415	0.18
0.4	0.5	0.462	0.21
0.4	0.8	0.535	1.4
0.4	1.4	0.659	1.4
0.4	2.0	0.791	2.1
2.0	0.0	0.2880	0.12
2.0	0.1	0.3095	0.12
2.0	0.2	0.3292	0.12
2.0	0.3	0.3480	0.12
2.0	0.5	0.3800	0.32
2.0	0.7	0.4090	0.32
2.0	1.0	0.4510	0.40
20.0	0.00	0.2385	0.14
20.0	0.02	0.2415	0.14
20.0	0.06	0.2450	0.21
20.0	0.09	0.2460	0.35
STA		0.7725	0.10

TABLE I. Parameters λ , A , and K (divided by N) at which simulations were carried out for the $N = 2$ chiral ϕ^4 model and the STA-Heisenberg model. Physical quantities were observed for every $C_{INT} \times L^2$ MCS.

λ	A	K/N	C_{INT}
0.4	0.00	0.3185	0.50
0.4	0.30	0.3660	0.60
0.4	0.60	0.4130	1.2
0.4	1.00	0.4700	1.8
0.4	2.00	0.6140	1.8
0.4	3.00	0.7556	3.0
2.0	0.3	0.3218	0.14
2.0	0.4	0.3328	0.21
2.0	0.5	0.3429	0.21
2.0	0.7	0.3624	0.35
2.0	1.0	0.3890	0.35
2.0	2.0	0.4640	1.5
4.0	0.00	0.2650	0.14
4.0	0.05	0.2725	0.14
4.0	0.10	0.2776	0.14
4.0	0.15	0.2833	0.14
20.0	0.00	0.242	0.14
20.0	0.07	0.247	0.14
20.0	0.10	0.247	0.21
20.0	0.13	0.247	0.21
$V_{3,2}$		0.2176	1.0
STA		1.17286	0.05

TABLE II. Parameters λ , A , and K (divided by N) at which simulations were carried out for the $N = 3$ chiral ϕ^4 model and the STA-Heisenberg model. Physical quantities were observed for every $C_{INT} \times L^2$ MCS.

λ	A	K/N	C_{INT}
1.0	2.0	0.3710	0.6
1.0	3.0	0.4100	0.8
1.0	4.0	0.4505	1.6
1.0	6.0	0.5270	2.4
2.0	1.0	0.3135	0.4
4.0	5.0	0.3355	0.4
4.0	8.0	0.3475	0.8
4.0	12.0	0.3584	1.2
4.0	20.0	0.3710	2.0
5.0	10.0	0.324	0.8
6.0	5.0	0.3012	0.6
6.0	8.0	0.3044	0.7
10.0	0.6	0.2675	0.15
10.0	1.0	0.2690	0.15
10.0	1.5	0.2700	0.15
10.0	2.0	0.2710	0.4
10.0	3.0	0.2718	0.4
10.0	5.0	0.2728	0.6
20.0	2.5	0.2525	0.6
100.0	0.1	0.2416	0.2
100.0	1.0	0.2380	2.0

TABLE III. Parameters λ , A , and K (divided by N) at which simulations were carried out for the $N = 8$ chiral ϕ^4 model. Physical quantities were observed for every $C_{INT} \times L^2$ MCS.